



Deposited via The University of Leeds.

White Rose Research Online URL for this paper:

<https://eprints.whiterose.ac.uk/id/eprint/103183/>

Version: Accepted Version

---

**Article:**

Wang, X, Luthi, SM, Hodgson, DM et al. (2017) Turbidite stacking patterns in salt-controlled minibasins: insights from integrated analogue models and numerical fluid flow simulations. *Sedimentology*, 64 (2). pp. 530-552. ISSN: 0037-0746

<https://doi.org/10.1111/sed.12313>

---

© 2016 The Authors. *Sedimentology* © 2016 International Association of Sedimentologists. This is the peer reviewed version of the following article: "Wang, X, Luthi, SM, Hodgson, DM, Sokoutis, D, Willingshofer, E and Groenenberg, RM (2016) Turbidite stacking patterns in salt-controlled minibasins: insights from integrated analogue models and numerical fluid flow simulations. *Sedimentology*", which has been published in final form at <http://dx.doi.org/10.1111/sed.12313>. This article may be used for non-commercial purposes in accordance with Wiley Terms and Conditions for Self-Archiving. Uploaded in accordance with the publisher's self-archiving policy.

**Reuse**

Items deposited in White Rose Research Online are protected by copyright, with all rights reserved unless indicated otherwise. They may be downloaded and/or printed for private study, or other acts as permitted by national copyright laws. The publisher or other rights holders may allow further reproduction and re-use of the full text version. This is indicated by the licence information on the White Rose Research Online record for the item.

**Takedown**

If you consider content in White Rose Research Online to be in breach of UK law, please notify us by emailing [eprints@whiterose.ac.uk](mailto:eprints@whiterose.ac.uk) including the URL of the record and the reason for the withdrawal request.

1     **TURBIDITE STACKING PATTERNS IN SALT-CONTROLLED MINBASINS:**  
2     **INSIGHTS FROM INTEGRATED ANALOGUE MODELS AND NUMERICAL**  
3                     **FLUID FLOW SIMULATIONS**

4  
5     XIAOXI WANG<sup>1</sup>, STEFAN M. LUTHI<sup>1</sup>, DAVID M. HODGSON<sup>2</sup>, DIMITRIOS  
6     SOKOUTIS<sup>3</sup>, ERNST WILLINGSHOFER<sup>3</sup>, REMCO M. GROENENBERG<sup>4</sup>

7     1. *Department of Geoscience and Engineering, Delft University of Technology,*  
8         *Stevinweg 1, 2628 CN Delft, The Netherlands (E-mail: s.m.luthi@tudelft.nl)*

9     2. *School of Earth and Environment, University of Leeds, Leeds, LS2 9JT, The United*  
10         *Kingdom*

11     3. *Department of Earth Sciences, Utrecht University, Budapestlaan 4, 3584 CD Utrecht,*  
12         *The Netherlands*

13     4. *Petrotechnical Data Systems, Lange Kleiweg 10, 2288 GK Rijswijk, The Netherlands*

14

15 **ABSTRACT**

16 The seafloor bathymetry of intraslope minibasins on passive continental margins plays a  
17 significant role in controlling turbidity current pathways and the resulting sediment  
18 distribution. The internal sediment stacking patterns remain poorly constrained due to the  
19 diversity of slope and minibasin configurations and the complicated interplay between  
20 turbidity current behaviour and evolving seafloor bathymetry. In this study, we combine  
21 laboratory analogue modelling of intraslope minibasin formation with numerical flow  
22 simulations of multi-event turbidity currents. This approach permits an improved  
23 understanding of evolving flow-bathymetry-deposit interactions and the resulting internal  
24 stacking patterns of the infills of such minibasins. The bathymetry includes a shelf-to-  
25 slope channel and an first minibasin separated by a confining ridge from two lower  
26 minibasins. The turbidity currents in the upper minibasin follow a series of stages from  
27 short initial ponding, filling-and-spilling and an extended transition to long  
28 retrogradational ponding. Upon reaching the minibasin floor the currents undergo a  
29 hydraulic jump, which greatly reduces their sediment-carrying capacity, and much  
30 sediment is deposited in the initial zone of subcritical flow. In the fill-and-spill stage,  
31 flow stripping and grain size partitioning allow the finer sediment to be transported  
32 across the confining ridge to lower areas that contain other minibasins. Overall, the  
33 sequences retrograde upstream with continued sedimentation due to longitudinal  
34 compensation accompanied by lateral switching into local depressions. Eventually, the  
35 basin infill retrogrades into the channel where cyclic steps with wavelengths of 1-2 km  
36 develop as a function of a pulsating flow. The results are at variance with conventional  
37 schemes that emphasise sequential downstream minibasin filling through ponding, and

38 they have important implications for locating the best reservoir-quality sands in the  
39 subsurface. Comparison of these results with published field and experimental examples  
40 seems to support the main conclusions.

41

42 **Keywords** Tectonic analogue modelling, numerical flow modelling, turbidity currents,  
43 intraslope minibasins, lateral compensation, longitudinal compensation, cyclic steps.

44

45 **INTRODUCTION**

46 Passive continental margins display a great diversity of seafloor bathymetries on their  
47 submarine slopes. In diapirically controlled settings, these bathymetries are characterized  
48 by numerous ridges and/or mini-basins, for example offshore the Gulf of Mexico (e.g.,  
49 Diegel et al., 1995; Rowan and Weimer, 1998; Prather, 2000; Lamb et al., 2006; Hudec et  
50 al., 2013), offshore West Africa (e.g., Duval et al., 1992; Liro and Coen, 1995; Marton et  
51 al., 2000; Hudec and Jackson, 2004; Brun and Fort, 2011), offshore Brazil (e.g.,  
52 Demercian et al., 1993; Cobbold et al., 1995; Roberts et al., 2004; Mohriak et al., 2012;  
53 Guerra and Underhill, 2012) and in the North Sea (e.g., Coward and Stewart, 1995;  
54 Kockel, 1998, Harding and Husse, 2015). Complicated seafloor bathymetries play a  
55 significant role in controlling turbidity current behaviour, sediment dispersal patterns and  
56 internal architectures of turbidite systems (Kneller and McCaffrey, 1999; McCaffrey and  
57 Kneller, 2001; Hodgson and Haughton, 2004; Gee and Gawthorpe, 2006; Lamb et al.,  
58 2006; Albertão et al., 2011, 2015; Oluboyo et al., 2014).

59

60 Concepts such as the fill-and-spill models (Winker 1996; Prather et al., 1998), the flow-  
61 stripping model (Sinclair and Tomasso 2002), and the silled sub-basins model and  
62 connected-tortuous-corridor model (Smith, 2004) have been proposed to explain and  
63 predict the filling history of successive intraslope minibasins. These models were  
64 developed from specific basin margins that are influenced by mud- or salt-diapirism, and  
65 they are conceptual because the architecture of basin infill could not be validated with  
66 high-resolution three-dimensional data. This lack of detail makes them difficult to apply  
67 to turbidite reservoirs in such settings.

68 Well-exposed outcrops with 3D control or high-resolution 3D seismic data could fill  
69 these resolution gaps, yet only few case studies contain such high quality data (Gervais et  
70 al., 2006; Moody et al., 2012). Most outcrops are two-dimensional and thus offer only  
71 partial information on the internal sedimentary architecture (Shanmugam and Moiola,  
72 1991; Shanmugam, 2000; Satur et al., 2000). 3D seismic data of sufficiently high  
73 resolution is sometimes available from the shallow subsurface but is often of lesser  
74 interest as it contains rarely natural resources. The present study aims i) to integrate  
75 analogue models and numerical simulations to investigate flow-bathymetry-deposit  
76 interactions during the filling of salt withdrawal minibasins; ii) to investigate the  
77 evolution of sedimentary dispersal and stacking patterns at a bed-scale resolution; and iii)  
78 to discuss similarities and differences with existing conceptual models of minibasin infill.

79 **METHODOLOGY**

80 This study adopts a novel method that integrates laboratory analogue modelling of  
 81 passive-margin seafloor bathymetries and numerical simulations of multiple turbidity  
 82 currents.

83

84 In a first step, laboratory analogue tectonic experiments using “sandbox” models  
 85 permitted realistic seafloor geomorphologies to be obtained that were digitized and  
 86 upscaled. The bathymetry serves as input surface for the numerical flow modeling, for  
 87 which the process-based FanBuilder software is used that simulates low-density turbidity  
 88 currents (Groenenberg et al., 2009, 2010). A series of parameters within ranges expected  
 89 to occur in nature constrained the flow simulations. Multiple flow events are run in a  
 90 single experiment such that the bathymetry continuously evolves with each new flow.  
 91 The resulting sedimentary sequences are then analyzed in 3-D in a series of strike and dip  
 92 sections, and as 1D pseudo-logs.

93

94 **ANALOGUE TECTONIC EXPERIMENTS**

95 “Sandbox” analogue experiments are widely used to model the evolution of a large  
 96 variety of deformation types in structural geology and tectonics (e.g., Colletta, et al.,  
 97 1991; Sokoutis and Willingshofer, 2011; Willingshofer et al., 2013). Analogue models  
 98 driven by gravitational forces have proven to be effective in helping to understand  
 99 deformation mechanisms caused by salt tectonics on passive continental margins such as  
 100 along the Gulf of Mexico and the South Atlantic margins (e.g., Vendeville and Cobbold,  
 101 1988; Cobbold and Szatmari, 1991; Vendeville and Jackson, 1992a, b; Brun and Fort,

102 2004, 2011). These margins are characterized by a transition from upslope extension to  
103 downslope compression caused by gravity sliding and spreading of the brittle-ductile  
104 package. In this study, the successful laboratory modeling of the Angolan passive margin  
105 conducted by Fort et al. (2004) and Brun and Fort (2004, 2011) has been taken for  
106 reference, and similar techniques and parameters are adopted here.

107

108 Silicone putty overlain by sand are used to represent the prekinematic salt and sediment  
109 respectively (Vendeville and Jackson, 1992a, b; Weijermars et al., 1993), while a plastic  
110 sheet placed under the silicone represents a weak décollement layer (McClay, 1990;  
111 Allemand and Brun, 1991). The silicone putty used is SGM-36 (Mark of Down Corning)  
112 with a density of about  $965 \text{ kg/m}^3$  and a viscosity of  $5 \times 10^4 \text{ Pa}\cdot\text{s}$ ; it is applied with a  
113 thickness of 8 mm. Weijermars (1986a, b, 1993) has demonstrated in a series of  
114 experiments the ability of this material to provide a rheologically-scaled analogue of salt.  
115 The overlying sand chosen here to represent the sedimentary sequence has a mean grain  
116 size of 0.3 mm, a density of about  $1500 \text{ kg/m}^3$  (uncompacted and in air) and a coefficient  
117 of friction of 0.9 without significant cohesion (Willingshofer et al., 2005); it is applied  
118 with a thickness of 10 mm. The model area is 50 cm wide and 120 cm long, with the sand-  
119 silicone layers resting on two linked horizontal plates that divide the model into two parts  
120 of 80 cm (Plate 1) and 40 cm (Plate 2) (Fig. 1). The experiment is started by tilting Plate  
121 1 to an angle of  $4^\circ$ . During the entire duration of the experiment, the layers are  
122 completely confined by metal bars on all sides. No sediment is added to the model in  
123 order to allow the formation of minibasins and ridges without them getting infilled with  
124 synkinematic sediments. A digital 3D laser installed above the model scans every 30

125 minutes the evolving topography, which simulates the seafloor bathymetry.. After 68  
 126 hours the tectonic structure was pronounced and judged to be realistic enough for the  
 127 experiment to be stopped (Fig. 2A).

128

129 The cross-section of the result displays three distinctive structural domains: extension,  
 130 translation and compression (Fig. 2B). In the upper part, well-developed extensional  
 131 structures formed, such as normal faults, grabens, minibasins and diapirs between rafts  
 132 (Fig. 2B). The maturity of the diapirs generally decreases downdip as a result of the  
 133 extensional structures in the upper slope area occurring earlier than those further downdip.  
 134 The transitional zone underwent a downward slab-like movement on the décollement  
 135 sheet. In the compressional domain, folds and thrusts are dominant and restricted to the  
 136 toe of the slope (Fig. 2B). The compressional domain migrates in both the downdip as  
 137 well as the updip direction, as can be deduced from the prograding directions of the folds  
 138 forming on both sides of the imbricated folds and thrusts.

139

140

#### 141 **THE INPUT BATHYMETRY**

142

143 The scanned 3D data of the uppermost, extensional domain (250 mm in the downdip  
 144 direction) of the final tectonic model forms the digital elevation model, which is upscaled  
 145 by a factor of  $8 \times 10^4$  with a cell size of 250 m. This increased the scale of the modelled  
 146 minibasin to a few to tens of kilometres in diameter, which are dimensions of typical  
 147 minibasins in nature (e.g., Hudec et al., 2009; Fort et al., 2004; Loncke et al., 2006). To  
 148 obtain a more realistic continental margin configuration and to reduce the boundary

149 effects, a shelf area with a width of 10 km and a gradient of slightly less than  $0.7^\circ$  is  
150 added upslope by Kriging interpolation. The model area (Fig. 3A) measures 15 km by 30  
151 km and contains an artificially imposed channel on the outer part of the shelf feeding  
152 downstream into an upper minibasin with confining slopes on all sides, followed by a  
153 slope-parallel ridge and several smaller minibasins that are followed again by a ridge (Fig.  
154 3B). The channel is slightly curved and has a U-shaped cross-section profile with an  
155 average thalweg slope of  $\approx 1.25^\circ$ . It is about 70 m deep, 3 km wide (with a 1.5 km wide  
156 thalweg) and 10 km long, and it connects to the upper minibasin, which is 10 km wide  
157 and 5 km long with an almost circular central area. At the downstream bounding edge of  
158 the upper minibasin there is a counterslope of  $\sim 1.20^\circ$  and a spillover point on the ridge  
159 that is about 60 m higher than the lowest point of the minibasin. The lee-side slope of the  
160 ridge is steeper with an average of  $\sim 2.60^\circ$ , leading directly to two smaller, poorly-  
161 confined minibasins of about 2.5 km in diameter that are adjacent to each other.

162

163

## 164 **FLOW SIMULATIONS**

165

166 “FanBuilder” is a three-dimensional process-based model that simulates turbidity current  
167 hydrodynamics and sedimentation on an arbitrary bathymetry over multiple successive  
168 flow events (Groenenberg, 2007; Groenenberg et al., 2009). FanBuilder possesses the  
169 following two important characteristics for this study: (1) it is designed to simulate low-  
170 density turbidity currents with Newtonian fluid behaviour and (2) geomorphic features  
171 and autogenic processes such as channelization, channel aggradation and avulsion, and  
172 lobe switching in the resulting deposits can be observed in real-time. The model is based

173 on five depth-averaged mathematical equations proposed by Parker et al. (1986). These  
174 five equations ensure the maintenance of flow momentum in the streamwise and  
175 transverse directions as well as flow mass and sediment mass conservation during one  
176 flow event but cannot handle higher-density currents above the Boussinesq  
177 approximation, i.e. with concentrations above about 7% in volume. A combined  
178 convection-diffusion equation governs sediment transport in this model. The model  
179 supports sediment transport of multiple grain-size classes and sediment exchange through  
180 erosion and deposition. The input parameters for the model include the initial bathymetry  
181 of the receiving basin, the grain size distribution of the sediment, the magnitude-  
182 frequency distribution of the flows, and the initial volume concentration of the sediment  
183 in the flows. By adjusting these parameters, their impact on the long-term stratigraphic  
184 evolution of successive turbidity current deposits can be simulated and studied. The  
185 evolution of the flows, such as the flow velocities, thicknesses and densities, and the  
186 densimetric Froude number, can be monitored in real time. The resulting stratigraphy in  
187 the form of the thickness and the mean grain size distribution of the deposits is  
188 instantaneously visible after each flow.

189

190 To ensure that FanBuilder is sufficiently realistic in simulating turbidity currents and  
191 their deposits, Groenenberg (2007) conducted two sets of validation experiments based  
192 on data from laboratory experiments. These included turbidity currents above a constant  
193 and smooth ramp by Luthi (1981) and experiments of turbidity currents encountering  
194 various shapes of obstacles by Kneller and McCaffrey (1995). The qualitative and  
195 quantitative comparison with these laboratory experiments were deemed sufficiently

196 good for FanBuilder to be applied to larger-scale simulations that include natural settings  
197 and volumetric sediment concentrations not exceeding 7% (Groenenberg, 2007;  
198 Groenenberg et al., 2009). The applications included the simulations of submarine lobes  
199 based on data from outcrops exposed in the Karoo Basin, South Africa (Groenenberg et  
200 al., 2010) as well as predictive models of the impact of relay ramps on turbidity current  
201 pathways with different inflow angles (Athmer et al., 2010). These successful  
202 applications of FanBuilder provided the incentive to use the software in the present study.

203

204

## 205 **NUMERICAL SIMULATION RESULTS**

206

207 The results reported here are from a set of 100 flow experiments whereby the inflow  
208 conditions were slightly supercritical as the densimetric Froude number lies just above 1,  
209 and in equilibrium as the resistance to flow is equal to the gravitational acceleration. The  
210 parameters to achieve these conditions include the flow velocity, the sediment  
211 concentration, the flow depth and the drag coefficient. Additional parameters defined  
212 include the initial flow width, the total released sediment volume and the grain size  
213 composition (Table 1). They are constrained within the range of magnitudes published  
214 from the few turbidity currents that have been measured in nature, which are exclusively  
215 from low concentration flows (Talling et al. 2015). Measurements in nature include  
216 turbidity currents on the Mid-Atlantic Ridge with a flow thickness of 30 m, a flow  
217 velocity of 1.5-40 m/s and a concentration of 0.03-0.12 (Van Andel and Komar, 1969);  
218 turbidity currents in the incised channel (without spillover lobes) of Bute Inlet with a

219 flow thickness of 30-40 m, a slope of 1.5°, a flow velocity of 3.35 m/s, a flow  
220 concentration of 0.005-0.01 and a maximum grain size of 0.480 mm (Zeng et al., 1991);  
221 four turbidity currents measured by Xu et al. (2004) with a flow-body thickness of 50 m  
222 and a maximum head velocity of 5-12 m/s along the canyon (Zeng and Lowe, 1997;  
223 Mulder and Alexander, 2001).

224

225 One hundred point-sourced flow events with identical flow parameters (Table 1) were run  
226 with the evolution of the flow and depositional characteristics monitored in real-time. For  
227 each flow the flow height, the densimetric Froude number, the depositional thickness and  
228 the mean grain size is recorded over the model area. Additionally, the total deposit  
229 thickness and average grain size of the entire sedimentary package was recorded. This  
230 allows for a continuous monitoring of the interplay between the evolving bathymetries,  
231 the flow behaviour, and the depositional characteristics.

232

233

#### 234 **Flow evolution**

235

236 The results of the hundred successive flow events show that four different stages of flow  
237 evolution can be distinguished. The flows are numbered 1 for the first one to 100 for the  
238 last one.

239

#### 240 *Initial ponding stage*

241 Full ponding of event 1 in the upper minibasin without any spill-over is observed (Fig. 4,  
 242 top). After about 3000s, the flow volume is completely released into the channel and  
 243 starts to enter the upper minibasin with a maximum flow velocity of about 6 m/s. After  
 244 reaching the minibasin centre, the flow expands and shortly thereafter a hydraulic jump  
 245 occurs, i.e. rapidly transitions from supercritical to subcritical, which decreases its  
 246 velocity and increases its height. The flow is not capable of breaching the counterslope  
 247 ridge and dissipates its entire energy in the upper minibasin.

248

249 ***Fill-and-spill stage***

250 Flows 2 to 31 partially spill over the downstream ridge confining the upper minibasin and  
 251 flow down the leeside slope into the lowermini-basins, most probably because the deposit  
 252 of flow event 1 had already reduced the depth of the minibasin enough to permit this.  
 253 Flow event 25 (Fig. 4, middle) is used as an example here to illustrate the flow evolution.  
 254 The flow expands in the upper minibasin with its flanks becoming subcritical. The central  
 255 part, however, does not undergo a hydraulic jump and remains supercritical and, due to  
 256 its high velocity, climbs up the counterslope and flows down into the lower minibasins  
 257 where the energy of the flow completely dissipates.

258

259 ***Transitional stage***

260 This stage encompasses flow events 32 to 40 and is characterized by irregular switching  
 261 between spill-over and minibasin-confined flows. Spill-over only happens in flow events  
 262 34, 36, 37 and 40 while in the remaining flows confinement prevails. This stage is  
 263 therefore transitional between the previous and the subsequent stages.

264

265 ***Retrogradational ponding stage***

266 For the remaining flows, from events 41 to 100, the turbidity currents are not able to spill  
267 over and remain trapped in the upper minibasin because retrogradational deposition on its  
268 counterslope ridge has accumulated to a level that is higher than the original ridge.  
269 Additionally, increasing deposition in the channel decreases the flow energy through a  
270 loss of sediment, but also through repeated hydraulic jumps caused by an increasingly  
271 irregular bathymetry. Figure 4 (bottom) illustrates this for the case of event 45.

272

273 **Flow-deposit interaction**

274 The deposits from the succession of flow events lead to an evolving bathymetric template  
275 that influences subsequent flow behavior. This in turn influences the sediment dispersal  
276 patterns, and notably the sediment thicknesses and grain sizes, with significant  
277 differences between the ponding, fill-and-spill and trapping stages.

278

279 ***Deposit and mean grain size***

280 The depositional thickness map of bed 1 (Fig. 5) indicates two sites of significant  
281 deposition. One is at the inflow where a levee-shaped deposit is formed with a maximum  
282 thickness of about 1.80 m. The other one is on the counterslope of the upper minibasin  
283 with a maximum thickness of about 1 m. Both locations also have the coarsest mean  
284 grain size (Fig. 5).

285

286 The beds formed during the fill-and-spill stage, illustrated by events 2, 20 and 30 in  
287 Figure 5, are distributed over three minibasins. The thickest sediment is located in the  
288 upper minibasin. Erosion occurs on the lee-side of the confining ridge (blue areas in Fig.  
289 5). In the early phase of this stage (e.g. bed 2), merely finer grains are transported to the  
290 lower minibasins by the spillover flows. Afterwards, the flows carry increasingly coarser  
291 grains over the bounding ridges to the lower minibasins, accompanied by stronger  
292 erosion on the downstream slope of the ridge (beds 20 and 30 in Fig. 5). The coarsest and  
293 thickest deposits are on the channel margins forming fledgling levees, the counterslopes  
294 of the three minibasins, and on the leeside of the bounding ridge.

295

296 At the transitional stage, spill-over becomes less frequent and eventually ceases. Even if  
297 the flows spill over, their grain size decreases downstream (bed 40 in Fig. 5), partly  
298 because deposition in the channel is seen to increase, forming very long-wavelength  
299 bedforms that contain some coarse material.

300

301 At the trapping stage, no deposition takes place in the lower minibasins. The  
302 accommodation in the upper minibasin is constantly shrinking (bed 60, 80 in Fig. 5) and  
303 the depocentre is moving upstream due to the back-stepping of the counterslope. The  
304 coarsest deposits are found in depressions in the channel spaced 1-2 kilometres apart  
305 where the flows become subcritical, while some minor erosion can be found in between  
306 them where the flows become supercritical (beds 80 and 100 in Fig. 5).

307

308 The thickness distribution of the entire 100-bed succession (Fig. 6) illustrates that the  
309 lower minibasins only received sediment during the first 40 flow events, while after that  
310 deposition was limited to the upper minibasin and the channel. The maximum deposit  
311 thickness is, however, found directly above the initial depocentre of the upper minibasin  
312 and amounts to slightly more than 80 m.

313

#### 314 **Bathymetric changes**

315 The bathymetric evolution is shown in three time slices corresponding to flow events 40,  
316 70 and 100 (Fig. 7). During the fill-and-spill stage, depositional ridges are seen to  
317 develop around the counterslope of the upper minibasin (Fig. 7A). They are obliquely  
318 orientated relative to the overall flow direction, probably caused by the complex  
319 interaction of large-scale vortices in the minibasin and backward flow from the  
320 counterslope (see e.g. flow 45 in Fig. 4). At the trapping stage, more depositional ridges  
321 form and divide the increasingly limited accommodation space into several segments.  
322 Similarly, the bedforms in the channel become more pronounced (Fig. 7B, C).

323 This evolution can also be observed in the longitudinal direction. Figure 7D shows that  
324 two internal ridges migrate upslope, starting around flow event 40, and increase in  
325 amplitude until they outgrow the original counterslope ridge of the upper minibasin.  
326 These ridges and the lowest bathymetric point shift upstream by 2 to 3 kilometres and  
327 grow such that effectively there are two spill points. The counterslope gradient changes  
328 through time too (Fig. 7E). Initially, the gradient decreases during the first 40 events  
329 when spill-over still occurred, and later increases from event 41 to event 50 when

330 trapping starts, and gradually decreases thereafter during the remainder of the trapping  
 331 stage (Fig. 7E).

332

333 **Depositional architecture**

334 The thickness and mean grains size distributions form the basis to subdivide the  
 335 stratigraphy resulting from the 100 flow events into seven bedding units. These are  
 336 related to the flow stages as follows: the initial ponding stage contains one Unit, the fill-  
 337 and-spill stage three, the transitional stage one, and the retrogradational ponding stage  
 338 two. Figure 8 shows the model area subdivided into five depositional zones (Fig. 8A) and  
 339 the proportional distribution of the seven bedding units for each of these zones (Fig. 8B).

340 With the exception of Unit 1, it is seen that the Units 2 to 7 show a steady regression  
 341 towards the upstream area, while the lower minibasins receive less sediment and  
 342 eventually become starved. The Units are subdivided according to their grain size and  
 343 thickness trends. Figure 9 summarizes the seven units in longitudinal and lateral cross-  
 344 sections, with their respective depocentres, defined here as the loci of greatest thickness,  
 345 indicated by dots in the three minibasins.

346

347 Unit 1, consists of only one bed, deposited 42% of the sediment in the minibasin, most of  
 348 it on the counterslope, with the remainder in the channel area.

349

350 Units 2 to 4 formed during the fill-and-spill phase. Unit 2, consists of beds formed by  
 351 events 2 to 11, has 20% of its deposit in the channel, 58% in the upper minibasin and 22%  
 352 in the lower minibasin area. The centre of the upper minibasin contains thin and fine-

353 grained beds with a coarsening- and thickening-upward trend while on the counterslope  
354 the beds are much thicker and coarser grained with a thinning-upward trend, In the two  
355 lower minibasins, this unit is thin-bedded and fine-grained with the depocentres off-  
356 centered due to run-up of the flows caused by the off-axial location of these minibasins.  
357 (Fig. 9). Unit 3 comprises beds 12 to bed 20 and its sediment volume distribution is  
358 similar to Unit 2 (Fig. 8). More coarse sediment is deposited in the upper minibasin,  
359 particularly in its centre, while the lower minibasins received finer grains with a  
360 continued asymmetric infill that exhibits longitudinal and lateral shifting. Unit 4 is the  
361 last sequence of the fill-and-spill stage and comprises beds 21 to 31. Here 60% of the  
362 sediment is deposited in the upper minibasin, while the lower minibasins received 17%  
363 with 23% in the channel. The continued retrogradation causes coarser grains and thicker  
364 beds to be deposited in the upper minibasin centre and finer grains in thinner beds on its  
365 counterslope. In the two lower minibasins, the fining- and thinning-upward trends  
366 continued concomitant with the upstream migration of the depocentre, and the lateral  
367 shift towards the minibasin centre. The depocentre of the upper minibasin longitudinally  
368 remained on the counterslope but retrograded, with a new ridge forming with a slight  
369 depression between it and the original ridge (Fig. 9). Laterally, the depocentre moves  
370 towards the basin centre.

371 Unit 5 is from the transitional stage and comprises beds from events 32 to 40. In the  
372 upper minibasin deposition on the counterslope practically ceased, with most sediment  
373 being deposited on the upstream side of the newly formed ridge and similar in character  
374 to Unit 4. The volume of sediment transported to the lower minibasins decreased  
375 considerably (Fig. 8) and becomes even finer with very thin beds.

376

377 Units 6 and 7 are from the retrogradational ponding stage. Unit 6 comprises beds from  
378 events 41 to 70. Because the flows were trapped in the upper minibasin, no sedimentation  
379 took place in the lower minibasins. Overall, deposition shifted towards the main channel  
380 and the inflow area (Fig. 8). Beds in the upper minibasin are finer-grained than in the  
381 underlying units, as much coarse material is trapped upstream. The depocentre moves  
382 upstream with a second ridge followed by a depression forming upstream, while laterally  
383 the depocentre moved further towards the basin centre (Fig. 9). Unit 7 is formed by beds  
384 from events 71 to 100. The main sedimentation moves further upstream with the  
385 depocentre now located in the lower channel area and deposition in the minibasin greatly  
386 decreased, with finer-grained and thinner beds than in the underlying units.

387

388

## 389 **DISCUSSION**

390

### 391 **Filling history**

392

393 Conceptual fill-spill-bypass models for successive mini-basins downslope have been  
394 invoked by numerous researchers (Winker, 1996; Weimer et al., 1998; Beaubouef and  
395 Friedman, 2000; Badalini et al., 2000; Sinclair and Tomasso 2002). In one commonly  
396 applied model, the highest minibasin is filled with sediments to spill point whereafter  
397 subsequent flows bypass sediments to the next, lower minibasin (Prather et al., 1998). By  
398 contrast, a flow-stripping model proposed by Badalini et al. (2000) suggests that

399 sequential minibasins could fill coevally. Sinclair and Tomasso (2002) described the four  
400 phases comprising this model as flow ponding, flow stripping, flow bypass and  
401 blanketing, basing their findings on flume experiments and outcrop studies. The results of  
402 the present study suggest that other filling modes are possible too. After an initial and  
403 very short-lived ponding phase, essentially two major phases are observed, the first one  
404 with partial spillover, and the second one with complete trapping in the highest minibasin.  
405 A transitional phase separated these two phases during which both flow modes occur.  
406 Thus, unlike previously reported models, the lower minibasins receive sediment in the  
407 initial phase of sedimentation and are thereafter cut-off from further sediment supply.  
408 The reason for this is the nature of the infill in the upper minibasin. Most sediment  
409 accumulates on the counterslope and from there retrogrades upstream while increasing  
410 the height of the ridge that separates it from the lower minibasins. Sedimentation on the  
411 counterslope occurs for two related reasons. Firstly, inertia carries the flows across the  
412 minibasin floor up the slope where they slow down and thus loose some of their sediment.  
413 Secondly, hydraulic jumps occur on the lower counterslope that increase the flow height  
414 but decrease the velocity and thus the transport capacity of the flows. The geometry of  
415 these hydraulic jumps, however, is complex as seen from the maps in Figure 4, with areas  
416 of super- and subcritical flow often occurring side-by-side. This is one of the main  
417 reasons for the laterally and longitudinally uneven basin infill pattern, as best  
418 demonstrated by the obliquely orientated ridges forming in the basin. It is the growth of  
419 these ridges with the associated retrogradational backstepping that leads to the reduction,  
420 and eventual cessation, of sediment supply from the lower minibasins.

421 Starting somewhere in the transitional phase, and perhaps initiated by the ridges, more  
422 hydraulic jumps occur in the upstream direction and eventually the entire channel is filled  
423 with bedforms and associated oscillations between super- and subcritical flow modes.  
424 These upstream migrating bedforms are interpreted as cyclic steps (Kostic and Parker,  
425 2006; Kostic, 2011), and have typical wavelengths of 1-2 km. Similar low-amplitude  
426 long-wavelength features have been reported from the Monterey East channel by Fildani  
427 et al. (2006), from the Squamish prodelta (Hughes Clarke et al., 2012), from the San  
428 Mateo Canyon channel system by Covault et al. (2014) and from Zhong et al. (2015) in  
429 the South Taiwan Shoal canyon. In most of these cases the wavelengths of the cyclic  
430 steps are even longer than the ones found here, but that is also the case for the overall  
431 scale of these channel systems. At the trapping stage, and particularly in its late phase  
432 (Unit 7), these cyclic steps cause much of the coarser sediment to be deposited in the  
433 channel, depriving the upper minibasin of high capacity flows and thus leading to  
434 increasingly thinner and finer-grained deposits there. Thus while during the spill-and-fill  
435 and transitional stages much coarse sediment reaches the three minibasins, in the trapping  
436 stage there is a continuous shift of the coarser-grained deposits upstream and into the  
437 channel and inflow area.

438 During the latest infill phase with strongly reduced accommodation, the asymmetric infill  
439 and lateral shifting of the depocentre caused by the hydraulic jumps leads to the  
440 formation of a depositional slightly leveed channel on the left flank of the upper  
441 minibasin (Fig. 9B). Had the experiments continued to a complete fill of the upper  
442 minibasin, this channel would have likely been the preferred pathway for sediment

443 bypass into the lower minibasins in a similar fashion as reported by Brunt et al. (2004)  
444 and Aas et al. (2010, 2014).

445 The important role of hydraulic jumps in the infill history of the minibasins could be  
446 argued to be a function of the boundary conditions of the model runs, and specifically of  
447 the supercritical inflow condition. Models performed with the same software and  
448 subcritical inflow conditions, however, indicate that the flows become supercritical after  
449 a short distance (Wang, 2015) and that the depositional history resembles the one  
450 described here.

451

#### 452 **Internal architecture and stacking pattern**

453

454 Much of the infill of the upper minibasin shows a thickening-then-thinning upward in  
455 parallel with a coarsening-then-fining succession. While this pattern could be interpreted  
456 to be the result of progradation-aggradation-retrogradation (Hodgson et al. ,2006), the  
457 succession observed is the result of the retrogradation of the entire depositional system.  
458 The lower succession comprises finer-grained and thinner beds deposited at the upstream  
459 tail end of the initial deposits. The central succession comprises coarser-grained and  
460 thicker beds deposited in the central part of the retrograding system, while the uppermost  
461 succession consists of finer-grained and thinner beds depositeds at the downstream end of  
462 flows. The entire flow-axial movement of the depositional system is described as  
463 longitudinal compensation, while the cross-sections perpendicular to flow suggest some  
464 degree of lateral compensation (Fig. 9). Although there are multiple internal shifts

465 between beds and units of beds, the maximum deposit thickness in the upper minibasin  
 466 lies exactly at the location of the lowest point in the original bathymetry (Fig. 6, right).  
 467 The lower minibasins show a thinning- and fining-upward trend caused by the reduction  
 468 of sediment supply as sediment is increasingly sequestered in the upper minibasin.  
 469 Eventually, when the upper minibasin is completely filled and flow bypass occurs, these  
 470 sequences would be overlain by coarser-grained deposits.

471

472 **Analogies with natural settings**

473

474 To validate the results obtained here sub-seismic observations from natural settings of  
 475 confined turbidite systems, either from outcrops or in the subsurface, would be required.  
 476 The large-scale lateral and longitudinal depositional shifts reported here would require  
 477 excellent continuous outcrops over large distances. Nevertheless, there are some  
 478 published data that the results reported here can be compared to. Moody et al. (2012)  
 479 examined the outcrops of the Morillo Formation of the Ainsa Basin (Spain) for spatial  
 480 and stratigraphic variations in geometry and dimensions of the channel elements in  
 481 weakly confined channel systems. They found that the axial downdip area has the highest  
 482 net sand content, which is similar to the results reported here where the coarser and  
 483 thicker deposits in the upper minibasin are also mainly in the axial-downdip area. Amy et  
 484 al. (2007, their figure 15) found a landward shift in the proximal depositional facies of a  
 485 sub-basin of the Alpine foreland in the Grès de Peira Cava (SE France). A similar  
 486 landward stacking pattern was obtained by process-based simulation of turbidity currents  
 487 over the recreated seafloor bathymetry of the Peira Cava turbidite system (Aas et al.,

488 2010, 2014). They offered two reasons that might contribute to this back-stepping pattern:  
489 (1) a net decline in sediment supply as a result of allogenic processes, and/or (2) a  
490 landward migration of the slope break. Their first hypothesis compares well with the  
491 insights gained here in that the sediment transported into the upper minibasin decreases  
492 due to an autogenic increase in deposition in the feeding channel. The second hypothesis  
493 was supported by evidence of an upward decrease of the slope-related facies. Finally, in  
494 an outcrop study of an exhumed intraslope lobe complex, Sychala et al. (2015)  
495 documented a landward shift in successive lobes related to the response to healing of  
496 transient accommodation above a partially filled slide scar.

497

498 Except for shallow high-frequency data, the reflection seismic method usually lacks the  
499 resolution to reveal the sedimentary details and small-scale stacking patterns needed to  
500 validate the results reported here. A typical seismic section of a salt-withdrawal  
501 minibasin shows an overall aggradational sequence in the minibasin centre (e.g., Winker,  
502 1996), although depocentres are known to migrate as salt welds start to develop.  
503 Moreover, surface and subsurface layers often experience post-depositional processes  
504 such as compaction and tectonic deformation that change their original geometry and  
505 architecture and thus make it even more difficult to unravel internal details. Using high-  
506 resolution seismic data, Gervais et al. (2006) recognized retrograding units on the  
507 depositional relief of the previous deposits in a distal lobe of the confined Golo turbidite  
508 system (latest Pleistocene, offshore Corsica). The suggested hydrodynamic reasons for  
509 this retrogradational pattern are similar to the ones offered here. Flows are erosive in the  
510 depression before an obstacle, but spread and deposit their sedimentary loads on its slope.

511 Progressively, therefore, deposition creates new frontal mounds that causes further  
 512 upstream stacking. Prather et al. (2012) documented the stratigraphic evolution of linked  
 513 intraslope basins in the Brazos-Trinity depositional systems (western Gulf of Mexico)  
 514 based on coring results and 3D seismic data. They focused on distinguishing the different  
 515 aprons (low-relief ponded, high-relief ponded and perched aprons) in these minibasins.  
 516 By carefully recognizing and tracing the depocentres of series 20-70 in basins II and IV, a  
 517 general trend of upstream migration can be obtained (Fig. 10), which to some extent  
 518 supports the upstream-stacking patterns in the modeling results presented here (Fig. 9).

519

520

521 **CONCLUSIONS**

522

523 A continental slope bathymetry with a feeder channel and minibasins separated by slope  
 524 parallel ridges obtained from laboratory “sandbox” modeling was used to study the flow  
 525 evolution and depositional infill by turbidity currents using a numerical process-based  
 526 method. An important result is that the flows initially partly spill over the confining ridge  
 527 of the uppermost minibasin, but that continued deposition modifies the bathymetry such  
 528 that sediment supply to the lower minibasins is shut off and the upper minibasin gets  
 529 filled retrogradationally, with the depocentres backstepping from the counterslope toward  
 530 the channel.. A complex distribution of the hydraulic jumps in the upper minibasin is  
 531 responsible for the development of complex internal ridges that move upstream and are  
 532 responsible for trapping coarser-grained material, resulting in a fining-upward trend in  
 533 the minibasin infill. These ridges probably induce supercritical to subcritical oscillations

534 in the flows that eventually lead to the development of cyclic steps along the entire  
535 channel length. The depositional retrogradation eventually fills the uppermost minibasin  
536 almost to spill, with increasing amounts of sediment being deposited in the channel,  
537 resulting in coarsening-upward sequences. There is some supporting evidence from  
538 outcrop and seismic data that the processes and depositional patterns identified here are  
539 described in natural systems where resolution allows.

540

541

542 **ACKNOWLEDGEMENTS**

543

544 Xiaoxi Wang is supported by the Chinese Scholarship Council and the Netherlands top  
545 research school ISES (Integrated Solid Earth Systems). We thank Remco Groenenberg  
546 for assistance with the FanBuilder flow modeling software.

547

548

549 **REFERENCES**

550

551 **Aas, T.E., Howell, J.A. Janocko, M., and Jackson, C.A.-L.** (2010) Control of Aptian  
552 palaeobathymetry on turbidite distribution in the Buchan Graben, Outer Moray Firth,  
553 Central North Sea. *Mar. and Petr. Geol.* **27**, 412–434.

554

555 **Aas, T.E., Basani, R., Howell, J. and Hansen, E.** (2014) Forward modelling as a  
556 method for predicting the distribution of deep-marine sands: an example from the Peira  
557 Cava Sub-Basin. In: *Sediment-Body Geometry and Heterogeneity: Analogue Studies for*  
558 *Modelling the Subsurface* (Eds. A.W. Martinius, J.A. Howell and T.R. Good), *Geol. Soc.*  
559 *Spec. Publ.* 387, 247–269.

560

561 **Albertão, G.A., Mulder, T. and Eschard, R.** (2011) Impact of salt-related  
562 palaeotopography on the distribution of turbidite reservoirs: Evidence from well-seismic  
563 analysis and structural restorations in Brazilian offshore. *Mar. and Petr. Geol.* **28**, 1023–  
564 1044.

565

566 **Albertão, G.A., Eschard, R., Mulder, T., Teles, V., Chauveau, B. and Joseph, P.**

567 (2015) Modelling the deposition of turbidite systems with Cellular Automata numerical  
568 simulations: a case study in the Brazilian offshore. *Mar. and Petr. Geol.* **59**, 166-186.

569

570 **Allemand, P. and Brun, J.P.** (1991) Width of continental rifts and rheological layering  
571 of the lithosphere. *Tectonophysics* **188**, 63–69.

572

573 **Amy, L.A., Kneller, B.C. and McCaffrey, W.D.** (2007). Facies architecture of the Gres  
574 de Peira Cava, SE France: landward stacking patterns in ponded turbiditic basins. *J. Geol.*  
575 *Soc.* **164**, 143–162.

576

577 **Athmer, W., Groenenberg, R.M., Luthi, S.M., Donselaar, M.E., Sokoutis, D. and**  
578 **Willigshofer, E.** (2010) Relay ramps as pathways for turbidity currents: a study  
579 combining analogue sandbox experiments and numerical flow simulations.  
580 *Sedimentology* **57**, 806–823.

581

582 **Badalini, G., Kneller, B. and Winker, C.D.** (2000) Architecture and processes in the  
583 Late Pleistocene Brazos-Trinity turbidite system, Gulf of Mexico Continental slope. In:  
584 *Deep-water reservoirs of the world* (Eds. P. Weimer, R.M. Slatt, J. Coleman, N.C. Rosen,  
585 H. Nelson, A.H. Bouma, M.J. Styzen and D.T. Lawrence), *Proceedings, 20th Annual*  
586 *Research Conference SEPM, Gulf Coast Section*, 304–317.

587

- 588 **Beauboeuf, R.T., and Friedmann, S.J.** (2000) High resolution seismic/sequence  
 589 stratigraphic framework for the evolution of Pleistocene intraslope basins, western Gulf  
 590 of Mexico: Depositional models and reservoir analogs. In: *Deep-water reservoirs of the*  
 591 *world* (Eds. P. Weimer, R.M. Slatt, J. Coleman, N.C. Rosen, H. Nelson, A.H. Bouma,  
 592 M.J. Styzen and D.T. Lawrence), *Proceedings, 20th Annual Research Conference SEPM,*  
 593 *Gulf Coast Section*, 40–60.
- 594
- 595 **Brun, J.P. and Fort, X.** (2004) Compressional salt tectonics (Angolan margin).  
 596 *Tectonophysics* **382**, 129–150.
- 597
- 598 **Brun, J.P. and Fort, X.** (2011) Salt tectonics at passive margins: geology versus models.  
 599 *Mar. and Petr. Geol.* **28**, 1123–1145.
- 600
- 601 **Brunt, R.L., McCaffrey, W.D. and Kneller, B.** (2004) Experimental modeling of the  
 602 spatial distribution of grain size developed in a fill-and-spill mini-basin setting. *J. Sed.*  
 603 *Res.* **74**, 438–446.
- 604
- 605 **Cobbold, P.R. and Szatmari, P.** (1991) Radial gravitational gliding on passive margins.  
 606 *Tectonophysics* **188**, 249–289.
- 607
- 608 **Cobbold, P.R., Szatmari, P., Demercian, L.S., Coelho, D. and Rossello, E.A.** (1995)  
 609 Seismic and experimental evidence for thin-skinned horizontal shortening by convergent  
 610 radial gliding on evaporites, deep-water Santos Basin, Brazil. In: *Salt tectonics: A global*

611 *perspective* (Eds. M.P.A. Jackson, D.G. Roberts and S. Snelson, S.), *AAPG Memoir* 65,  
612 305–321.

613

614 **Colletta, B., Letouzey, J., Pinedo, R., Ballard, J.F. and Balé, P.** (1991) Computerized  
615 X-ray tomography analysis of sandbox models: Examples of thin-skinned thrust systems.  
616 *Geology* **19**, 1063–1067.

617

618 **Coward, M. and Stewart, S.** (1995) Salt-influenced structures in the Mesozoic–Tertiary  
619 cover of the southern North Sea, U.K. In: *Salt tectonics: a global perspective* (Eds.  
620 M.P.A. Jackson, D.G. Roberts and S. Snelson) *AAPG Memoir* 65, 229–250.

621

622 **Demercian, S., Szatmari, P. and Cobbold, P.R.** (1993) Style and pattern of salt diapirs  
623 due to thin-skinned gravitational gliding, Campos and Santos Basins, offshore Brazil.  
624 *Tectonophysics* **228**, 393–433.

625

626

627 **Diegel, F.A., Karlo, J.F., Schuster, D.C., Shoup, R.C. and Tauvers P.R.** (1995)  
628 Cenozoic structural evolution and tectonostratigraphic framework of the northern Gulf  
629 Coast continental margin. In: *Salt tectonics: a global perspective* (Eds. M.P.A. Jackson,  
630 D.G. Roberts and S. Snelson) *AAPG Memoir* 65, 109–151.

631

632 **Duval, B., Cramez, C. and Jackson, M.P.A.** (1992) Raft tectonics in the Kwanza Basin,  
633 Angola. *Mar. and Petr. Geol.* **9**, 389–404.

634

635 **Fildani, A., Normark, W.R., Kostic, S. and Parker, G.** (2006) Channel formation by  
 636 flow stripping: large-scale scour features along the Monterey East Channel and their  
 637 relation to sediment waves: *Sedimentology* **53**, 1265–1287.

638

639 **Fort, X., Brun, J.P. and Chauvel, F.** (2004) Salt tectonics on the Angolan margin,  
 640 synsedimentary deformation processes. *AAPG Bull.* **88**, 1523–1544.

641

642 **Gee, M.J.R. and Gawthorpe, R.L.** (2006) Submarine channels controlled by salt  
 643 tectonics: examples from 3D seismic data offshore Angola. *Marine and Petroleum*  
 644 *Geology* **23**, 443-458.

645

646 **Gervais, A., Savoye, B., Mulder, T. and Gonthier, E.** (2006) Sandy modern turbidite  
 647 lobes: A new insight from high resolution seismic data. *Mar. and Petr. Geol.* **23**, 485–  
 648 502.

649

650 **Groenenberg, R.M.** (2007) *Process-based modelling of turbidity-current hydrodynamics*  
 651 *and sedimentation*. Ph.D. thesis, Delft University of Technology, 200 p.

652

653 **Groenenberg, R.M., Sloff, C.J. and Weltje, G.J.** (2009) A high-resolution 2-DH  
 654 numerical scheme for process-based modelling of 3-D turbidite fan stratigraphy.  
 655 *Computers and Geosciences* **35**, 1686–1700.

656

- 657 **Groenenberg, R.M., Hodgson, D.M., Pr lat, A., Luthi, S.M. and Flint, S.** (2010)  
 658 Flow-deposit interactions in submarine lobes: insights from outcrop observations and  
 659 realizations of a process-based numerical model. *J. Sed. Res.* **80**, 252–267.  
 660
- 661 **Guerra, M.C.M. and Underhill, J.R.** (2012) Role of halokinesis in controlling structural  
 662 styles and sediment dispersal in the Santos basin, offshore Brazil. In: *Salt Tectonics,*  
 663 *Sediments, Prospectivity* (Eds. G.I. Alsop, S.G. Archer, A.J. Hartley, N.T. Grant and R.  
 664 Hodgkinson), *Geol. Soc. London Spec. Publ.* 363, 163–206.  
 665
- 666 **Harding, R. and Husse, M.** (2015) Salt on the move: Multi stage evolution of salt diapirs  
 667 in the Netherlands North Sea. *Mar. and Petr. Geol.* **61**, 39-55.  
 668
- 669 **Hodgson, D.M. and Haughton, P.D.W.** (2004) Impact of syndepositional faulting on  
 670 gravity current behavior and deep-water stratigraphy: Tabernas-Sorbas Basin, SE Spain.  
 671 In: *Confined Turbidite Systems* (Eds. S.A. Lomas and P. Joseph), *Geol. Soc. Spec. Publ.*  
 672 222, 135–158.  
 673
- 674 **Hodgson, D.M., Flint, S.S., Hodgetts, D., Drinkwater, N.J., Johannessen, E.P. and**  
 675 **Luthi, S.M.** (2006) Stratigraphic evolution of fine-grained submarine fan systems,  
 676 Tanqua depocentre, Karoo Basin, South Africa. *J. Sed. Res.* **76**, 20-40.  
 677

678 **Hudec, M.R. and Jackson, M.P.A.** (2004) Regional restoration across the Kwanza Basin,  
 679 Angola: Salt tectonics triggered by repeated uplift of a metastable passive margin. *AAPG*  
 680 *Bull.* **88**, 971–990.

681

682 **Hudec, M.R., Jackson, M.P.A. and Schultz-Ela, D.D.** (2009) The paradox of minibasin  
 683 subsidence into salt: clues to the evolution of crustal basins. *Geol. Soc. Am. Bull.* **121**,  
 684 201–221.

685

686 **Hudec, M.R., Jackson, M.P.A. and Peel, F.J.** (2013) Influence of deep Louann structure  
 687 on the evolution of the northern Gulf of Mexico. *AAPG Bull.* **10**, 1711–1735.

688

689 **Kneller, B.C. and McCaffrey, W.D.** (1995) Modelling the effects of salt-induced  
 690 topography on deposition from turbidity currents. In: *Salt, Sediment and Hydrocarbons*  
 691 (Eds. C.S. Travis, H. Harrison, M.R. Hudec, B.C. Vendeville, F.S. Peel and B.E. Perkins),  
 692 *Proceedings, 16th Annual Research Conference SEPM, Gulf Coast Section*, 137–145.

693

694 **Kneller, B.C. and McCaffrey, W.D.** (1999) Depositional effects of flow non-uniformity  
 695 and stratification within turbidity currents approaching a bounding slope: deflection,  
 696 reflection and facies variation. *J. Sed. Res.* **69**, 980–991.

697

698 **Kockel, F.** (1998) Salt problems in Northwest Germany and the German North Sea  
 699 sector. In: *Geology and Geophysics of Salt Structures* (Eds. F. Kockel and R. Marschall,  
 700 R.). *J. Seism. Expl.* **7**, 219–235.

701

702 **Kostic, S.** (2011) Modeling of submarine cyclic steps: Controls on their formation,  
703 migration, and architecture. *Geosphere* **7**, 294–304.

704

705 **Kostic, S., and Parker, G.** (2006) The response of turbidity currents to a canyon–fan  
706 transition: Internal hydraulic jumps and depositional signatures. *J. Hydr. Res.* **44**, 631–  
707 653.

708

709 **Lamb, M.P., Toniolo, H. and Parker, G.** (2006) Trapping of sustained turbidity currents  
710 by intraslope minibasins. *Sedimentology* **53**, 147–160.

711

712 **Liro, L.M. and Coen, R.** (1995) Salt deformation history and postsalt structural trends,  
713 offshore southern Gabon, west Africa. In: *Salt tectonics: a global perspective* (Eds.  
714 M.P.A. Jackson, D.G. Roberts and S. Snelson) *AAPG Memoir*, 65, 323–331.

715

716 **Loncke, L., Gaullier, V., Mascle, J., Vendeville, B. and Camera, L.** (2006) The Nile  
717 deep-sea fan: an example of interacting sedimentation, salt tectonics, and inherited  
718 subsalt paleotopographic features. *Mar. and Petr. Geol.* **23**, 297–315.

719

720 **Luthi, S.M.** (1981) Experiments on non-channelized turbidity currents and their deposits.  
721 *Marine Geology* **40**, M59–M68.

722

723 **Marton, L.G., Tari, G.C. and Lehmann, C.T.** (2000) Evolution of the Angolan passive  
724 margin, West Africa, with emphasis on post-salt structural styles. In: *Atlantic rifts and*  
725 *continental margins* (Eds. W.U. Mohriak and M. Talwani). *AGU Geophysical*  
726 *Monograph* 115, 129–149.

727

728 **McCaffrey, W.D. and Kneller, B.C.** (2001) Process controls on the development of trap  
729 potential on the margins of confined turbidite systems and aid to reservoir evaluation.  
730 *AAPG Bull.* **85**, 971–988.

731

732 **McClay, K.R.** (1990) Extensional fault systems in sedimentary basins: a review of  
733 analogue model studies. *Mar. and Petr. Geol.* **7**, 206–233.

734

735 **Mohriak, W.U., Azatmari, P. and Anjos, S.** (2012) Salt: geology and tectonics of  
736 selected Brazilian basins in their global context. In: *Salt Tectonics, Sediments,*  
737 *Prospectivity* (Eds. G.I. Alsop, S.G. Archer, A.J. Hartley, N.T. Grant and R. Hodgkinson),  
738 *Geol. Soc. London Spec. Publ.* 363, 131–158.

739

740 **Moody, J.D., Pyles, D.R., Clark, J. and Bouroullec, R.** (2012) Quantitative outcrop  
741 characterization of an analog to weakly confined submarine channel systems: Morillo 1  
742 Member, Ainsa Basin, Spain. *AAPG Bull.* **96**, 1813–1841.

743

- 744 **Oluboyo, A.P., Gawthorpe, R.L., Bakke, K. and Hadler-Jacobsen, F.** (2014) Salt  
 745 tectonic control on deep-water turbidite depositional systems: Miocene, southwestern  
 746 Lower Congo Basin, offshore Angola. *Basin Res.* **26**, 597–620.  
 747
- 748 **Parker, G., Fukushima, Y. and Pantin, H.M.** (1986) Self-accelerating turbidity currents.  
 749 *J. Fluid. Mech.* **171**, 145–181.  
 750
- 751 **Prather, B.E., Booth, J.R., Steffens, G.S. and Craig, P.A.** (1998) Classification,  
 752 lithologic calibration, and stratigraphic succession of seismic facies of intraslope basins,  
 753 deep-water Gulf of Mexico. *AAPG Bull.* **82**, 701–728.  
 754
- 755 **Prather, B.E.** (2000) Calibration and visualization of depositional process models for  
 756 above-grade slopes: A case study from the Gulf of Mexico. *Mar. and Petr. Geol.* **17**,  
 757 619–638.  
 758
- 759 **Prather, B.E., Pirmez, C. and Winker, C.D.** (2012) Stratigraphy of linked intraslope  
 760 basins: Brazos-Trinity system western Gulf of Mexico. *SEPM Spec. Publ.* **99**, 83–109.  
 761
- 762 **Roberts, M.J., Metzgar, C.R., Liu, J. and Lim, S.J.** (2004) Regional assessment of salt  
 763 weld timing, Campos Basin, Brazil. In: *Salt-sediment interactions and hydrocarbon*  
 764 *prospectivity: Concepts, applications, and case studies for the 21st Century* (Eds. P.J.  
 765 Post, D.L. Olson, K.T. Lyons, S.L. Palmes, P.F. Harrison and N.C. Rosen), *Proceedings*,  
 766 *24th Annual Research Conference SEPM, Gulf Coast Section*, 371–389.

767

768 **Rowan, M.G. and Weimer, P.** (1998) Salt-sediment interaction, central Louisiana outer  
769 shelf and upper slope, northern Gulf of Mexico. *AAPG Bull.* **82**, 1055–1082.

770

771 **Satur, N., Hurst, A., Cronin, B.T., Kelling, G. and Gürbüz, K.** (2000) Sand body  
772 geometry in a sand-rich, deep-water clastic system, Miocene Cingöz Formation of  
773 southern Turkey. *Mar. and Petr. Geol.* **17**, 239–252.

774

775 **Shanmugam, G. and Moiola, R.J.** (1991) Types of submarine fan lobes: models and  
776 implications. *AAPG Bull.* **75**, 156–179.

777

778 **Shanmugam, G.** (2000) 50 years of the turbidite paradigm (1950s–1990s): deep-water  
779 processes and facies models. *Mar. and Petr. Geol.* **17**, 85–342.

780

781 **Sinclair H.D. and Tomasso, M.** (2002) Depositional evolution of confined turbidite  
782 basins. *J. Sed. Res.* **72**, 451–456.

783

784 **Smith, R.** (2004) Silled sub-basins to connected tortuous corridors: sediment distribution  
785 systems on topographically complex sub-aqueous slopes. In: *Confined Turbidite Systems*  
786 (Eds. S.A. Lomas and P. Joseph), *Geol. Soc. Spec. Publ.* **222**, 23–44.

787

788 **Sokoutis, D. and Willingshofer, E.** (2011) Decoupling during continental collision and  
789 intraplate deformation. *Earth and Planet. Sci. Let.* **305**, 435–444.

790

791 **Spychala, Y.T., Hodgson, D.M., Flint, S.S. and Mountney, N.** (2015) Constraining the  
 792 sedimentology and stratigraphy of submarine intraslope lobe deposits using exhumed  
 793 examples from the Karoo Basin, South Africa. *Sedimentary Geology*, **322**, 67-81.

794

795 **Talling, P.J.; Allin, J.; Armitage, D.A.; Arnott, R.W.C.; Cartigny, M.J.B.; Clare,**  
 796 **M.A.; Felletti, F.; Covault, J. A.; Girardclos, S.; Hansen, E.; Hill, P.R.; Hiscott, R.N.;**  
 797 **Hogg, A.J.; Clarke, J.H.; Jobe, Z.R.; Malgesini, G.; Mozzato, A.; Naruse, H.;**  
 798 **Parkinson, S.; Peel, F.J.; Piper, D.J.W.; Pope, E.; Postma, G.; Rowley, P.; Sguazzini,**  
 799 **A.; Stevenson, C.J.; Sumner, E.J.; Sylvester, Z.; Watts, C. and Xu, J.** (2015) Key  
 800 future directions for research on turbidity currents and their deposits. *J. Sed. Res.* **85**. 153-  
 801 169.

802

803 **Van Andel, T.H. and Komar, D.** (1969) Ponded sediments of the Mid-Atlantic Ridge  
 804 between 22° and 23° North Latitude. *Geol. Soc. Am. Bull.* **80**, 1163–1190.

805

806 **Vendeville, B.C. and Cobbold, P.R.** (1988) How normal faulting and sedimentation  
 807 interact to produce listric fault profiles and stratigraphic wedges. *J. of Struct. Geol.* **10**,  
 808 649–659.

809

810 **Vendeville, B.C. and Jackson, M.P.A.** (1992a). The rise of diapirs during thin-skinned  
 811 extension. *Mar. and Petr. Geol.* **9**, 331–353.

812

813 **Vendeville, B.C. and Jackson, M.P.A.** (1992b) The fall of diapirs during thin-skinned  
814 extension. *Mar. and Petr. Geol.* **9**, 354–371.

815

816 **Wang, X.** (2015) *Turbidite flows and their deposits on slopes with minibasins*. Ph.D.  
817 thesis, Delft University of Technology, 184 p.

818

819 **Weijermars, R.** (1986a) Finite strain of laminar flows can be visualized in SGM36-  
820 polymer. *Naturwissenschaften* **73**, 33–34.

821

822 **Weijermars, R.** (1986b) Flow behaviour and physical chemistry of bouncing putties and  
823 related polymers in view of tectonic laboratory applications. *Tectonophysics* **124**, 325–  
824 358.

825

826 **Weijermars, R., Jackson, M.P.A. and Vendeville, B.** (1993) Rheological and tectonic  
827 modeling of salt provinces. *Tectonophysics* **217**, 143–174.

828

829 **Weimer, P., Varnai, P., Budhijanto, F.M., Acosta, Z. M., Martinez, R.E., Navarro,**  
830 **A.F., Rowan, M.G., McBride, B.C., Villamil, T., Arango, C., Crews, J.R. and Pulham,**  
831 **A.J.** (1998) Sequence stratigraphy of Pliocene and Pleistocene turbidite systems, northern  
832 Green Canyon and Ewing Bank (offshore Louisiana), northern Gulf of Mexico. *AAPG*  
833 *Bull.* **82**, 918–960.

834

- 835 **Willingshofer, E., Sokoutis, D. and Burg, J.-P.** (2005) Lithospheric-scale analogue  
836 modeling of collision zones with a pre-existing weak zone. *Geol. Soc. Spec. Publ.* 243,  
837 277-294.  
838
- 839 **Willingshofer, E., Sokoutis, D., Luth, S.W., Beekman, F. and Cloetingh, S.** (2013)  
840 Subduction and deformation of the continental lithosphere in response to plate and crust-  
841 mantle coupling. *Geology* **41**, 1239-1242.  
842
- 843 **Winker, C.D.** (1996) High-resolution seismic stratigraphy of a Late Pleistocene  
844 submarine fan ponded by salt-withdrawal mini-basins on the Gulf of Mexico continental  
845 slope. *Proceedings, Offshore Technology Conference*, 619–628.  
846
- 847 **Xu, J.P., Noble, M.A. and Rosenfeld, L.K.** (2004) In-situ measurements of velocity  
848 structure within turbidity currents. *Geophys. Res. Let.* 31 (9).  
849
- 850 **Zeng, J., Lowe, D. R., Prior, D. B., Wisenam, W. J., Jr, and Bornhold, B. D.** (1991)  
851 Flow properties of turbidity currents in Bute inlet, British Columbia. *Sedimentology* **38**,  
852 975–996.  
853
- 854 **Zhong, G., Cartigny, M.J.B., Kuang, Z. and Wang, L.** (2015) Cyclic steps along the  
855 South Taiwan Shoal and West Penghu submarine canyons on the northeastern continental  
856 slope of the South China Sea. *Bull. Geol. Soc. Am.* **127**, 804-824.  
857

858 **FIGURE CAPTIONS**

859 **Fig. 1.** Setup of the sand-silicone experiment. A: Oblique top views showing the model  
 860 set-up, the dimensions and the boundary confinements. B: Longitudinal cross-section of  
 861 the model showing the internal layering. Plate 1 is tilted at an angle  $\alpha = 4^\circ$  to initiate the  
 862 experiment.

863

864 **Fig. 2.** A: An artificial illumination of the sand-silicone experiment after 68 hours.  
 865 Structural elements are indicated as follows: D = Diapir; Fd = Fold; T = Thrust; MB =  
 866 Minibasin. B: Longitudinal cross-section, with the three main structural domains and the  
 867 location of the minibasins indicated.

868

869 **Fig. 3.** A: 3D view of the topographic area used in this study as the seabed bathymetry  
 870 analogue. The main geomorphological elements include (a) a leveed channel, (b) a well-  
 871 confined minibasin, (c) diapiric ridges and (d) two poorly-confined minibasins. The blue  
 872 arrow indicates the inflow point and the initial direction of the simulated turbidity  
 873 currents. The vertical exaggeration is 20x. B: Plan view contour map of the same area  
 874 with red hues indicating the slope angles as the steepest descent or ascent at any grid  
 875 node on the surface. Blue arrow indicates upslope entry point.

876

877 **Fig. 4.** Flow evolution of events 1, 25 and 45, representative for the initial ponding stage,  
 878 the fill-and-spill stage, and the retrogradational ponding stage. Shown are the flow  
 879 thicknesses, the velocity vectors and the densimetric Froude number (only as being  
 880 super- or subcritical). The time slices were chosen to illustrate the main phases of these

881 three flows and are therefore not equal for the three experiments. Note that flow event 25  
 882 lasted 2.5 hours until the last sediment had settled; the ponding flows were in general  
 883 shorter lived. In event 45 the hydraulic jumps in the channel can be seen.

884

885 **Fig. 5.** Maps showing the bed thicknesses and mean grain sizes (grouped into four  
 886 categories) for the beds resulting from flow events 1, 2, 20, 30, 40, 60, 80 and 100. The  
 887 extended depositional area is well seen in beds 2, 20 and 30, with some coarse sediment  
 888 reaching the lower minibasins but also forming levees. Areas of net erosion, shown in  
 889 blue on the bed thickness maps, occur in the channel and the leeside of the confining  
 890 ridge. Bed 40 already shows the retrogradational development, which continues in beds  
 891 60, 80 and 100 where the cyclic steps are clearly seen.

892

893 **Fig. 6.** Maps showing the depositional thicknesses of the beds formed in the fill-and-  
 894 spill-dominated phase (events 2-40), the ponding-dominated stage (events 41-100) and  
 895 the total depositional thickness of all 100 events. Note that the thickness colour scale bar  
 896 changes in each map.

897

898 **Fig. 7.** Artificially illuminated maps showing the bathymetries after events 40 (A), 70 (B)  
 899 and 100 (C). Notice that there are no changes downstream of the upper minibasin as these  
 900 snapshots are all from the retrogradational ponding stage. D: The bathymetric evolution  
 901 of the upper minibasin in a longitudinal cross-section along the line indicated in C, in  
 902 steps of 10 flow events. Round dots indicate potential “spill points” of the upper  
 903 minibasin while black squares indicate the location of the lowest points in the sections.

904 This cross-section illustrates that the latter differ substantially from the depocentres. E:  
 905 The average counterslope gradient, defined here as the angle from the lowest point to the  
 906 “spill-over point”. It shows a decrease during the fill-and-spill-dominated phase then a  
 907 jump to a much higher gradient as a basin-internal ridge becomes the new spill-point, and  
 908 from there throughout the ponding-dominated phase again a monotonic decrease of the  
 909 gradient.

910

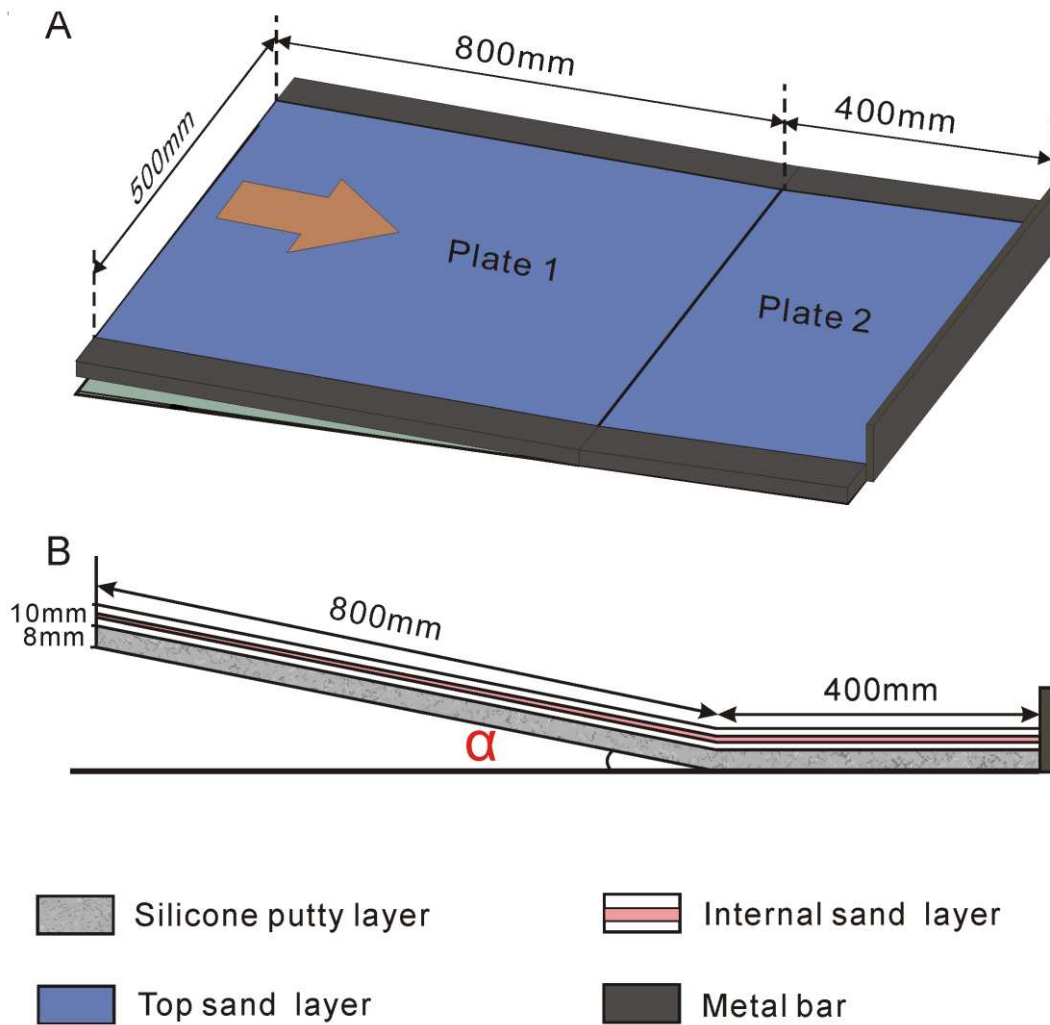
911 **Fig. 8.** A: The spatial division of the bathymetry into five depositional domains. The  
 912 leeward side of the confining ridge contains only very minor deposits and is not  
 913 considered here. B: Proportion of the sediment volumes in the five domains for the seven  
 914 depositional units, with U1 belonging to the initial ponding stage, U2-U4 to the fill-and-  
 915 spill stage, U5 to the transitional stage, and U6-U7 to the retrogradational ponding stage.  
 916 Notice the relatively constant sediment distribution in the fill-and-spill stage and the  
 917 continuous backstepping thereafter.

918

919 **Fig. 9.** Longitudinal (A-A') cross-section along the main flow axis shown in the insert,  
 920 with the colours indicating the tops of the seven depositional units and the dots their  
 921 respective depocentres. Notice the general upstream migration, for the last unit even in a  
 922 punctuated jump. This longitudinal compensation contrasts with the lateral compensation  
 923 exhibited in all three minibasins, as shown in the across-flow cross-section for the upper  
 924 minibasin (B-B'), the first lower minibasin (C-C') and the second lower minibasin (D-D').

925

926 **Fig. 10.** Stratigraphic evolution of basins II and IV in the Brazos-Trinity depositional  
 927 system (modified from Prather et al., 2012), with the colours representing the different  
 928 interpreted depositional series. Black dots indicate the interpreted depocentres of each  
 929 series. After the first two units shown in pink and dark blue the two minibasins had  
 930 reached approximately their present shape, so salt tectonics are considered a minor  
 931 influence in the backstepping of the depocentres.

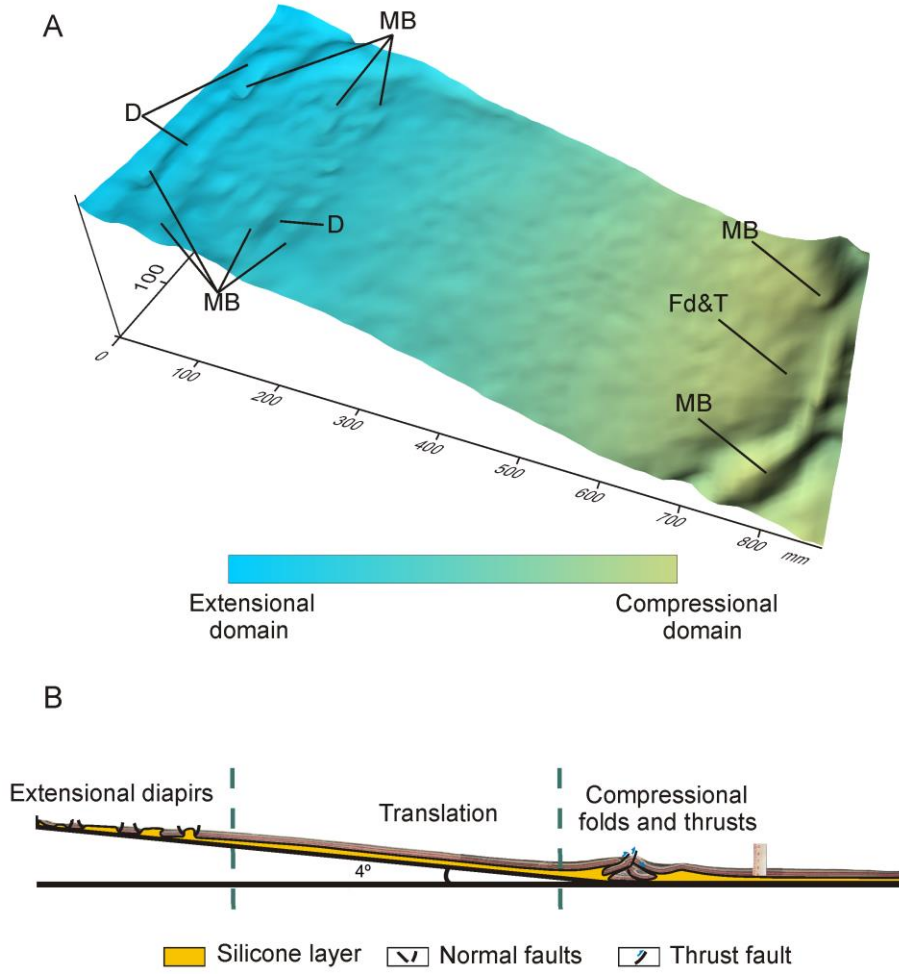


932

933 **Figure 1**

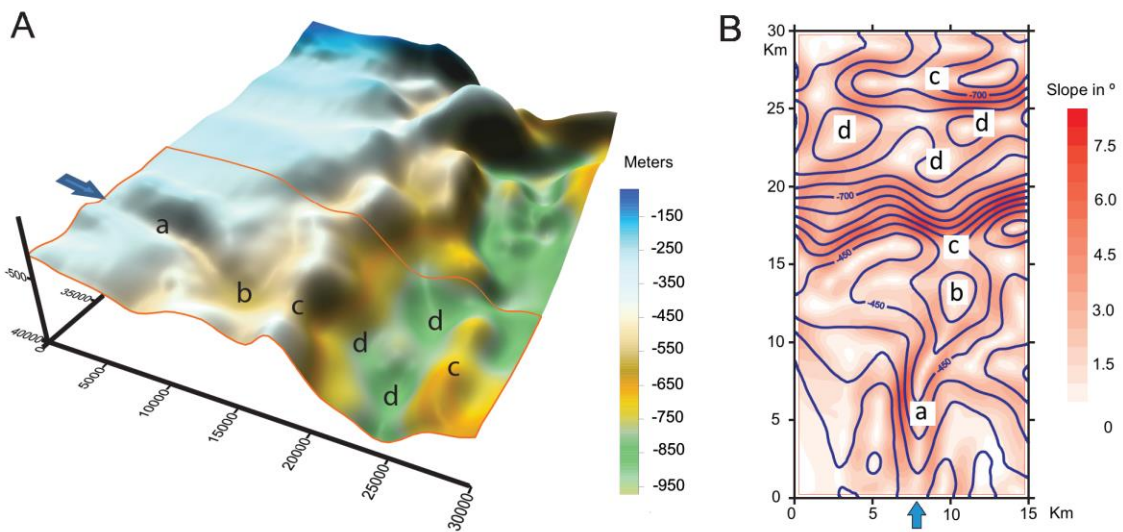
934

MODELLING THE STRATIGRAPHIC ARCHITECTURE OF MINIBASINS



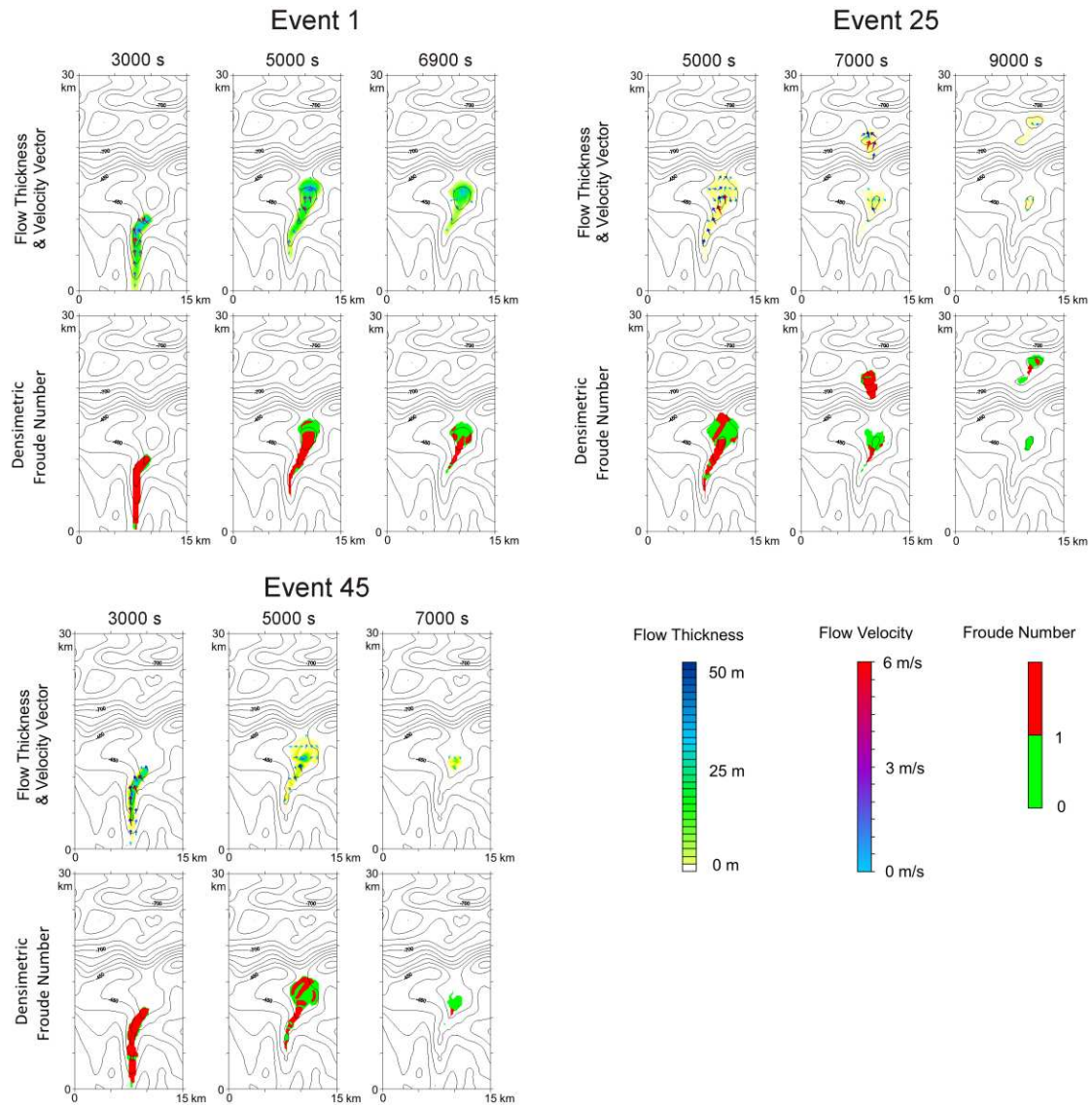
935

936 **Figure 2**



937

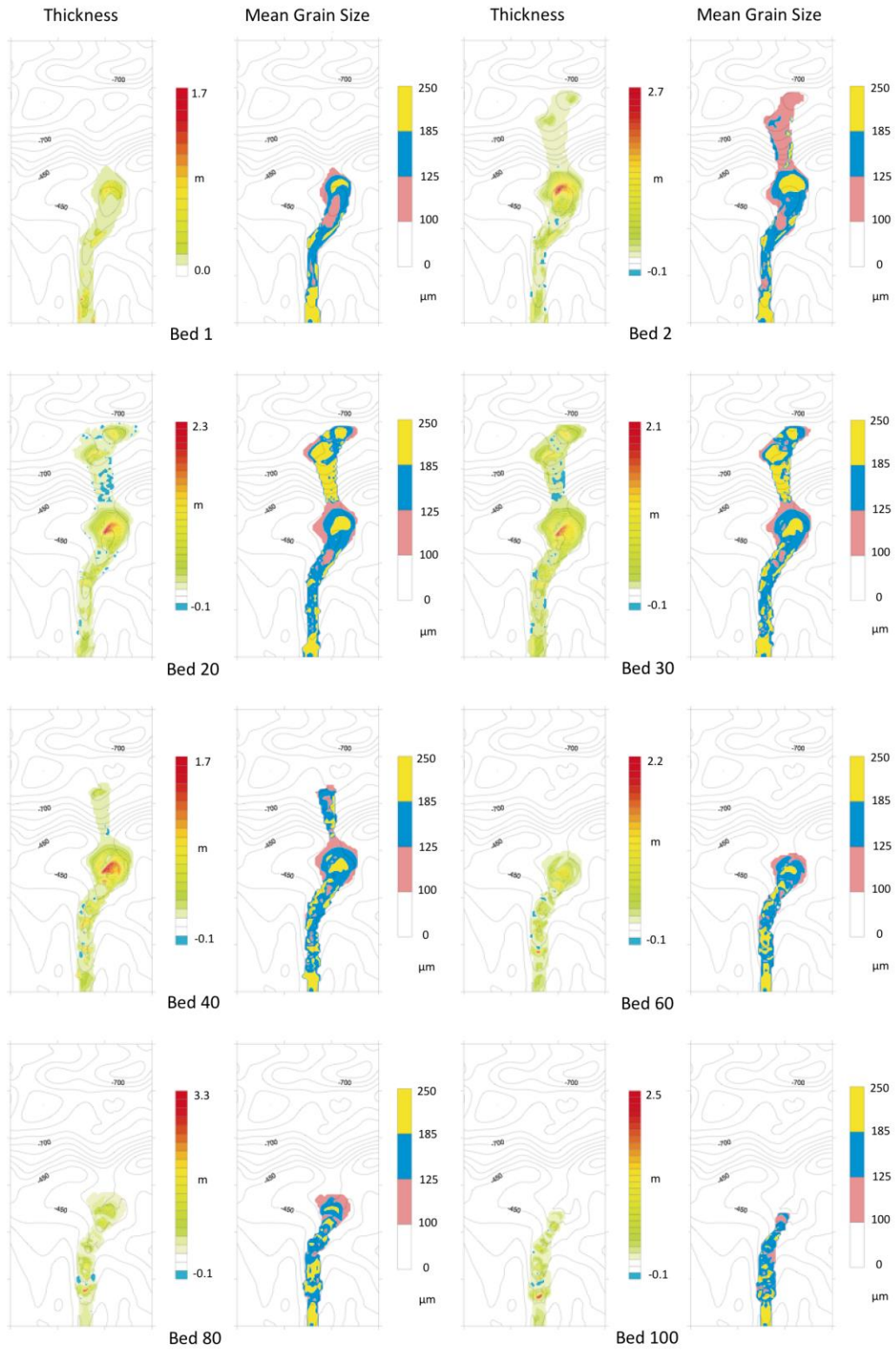
938 **Figure 3**



939

940 **Figure 4**

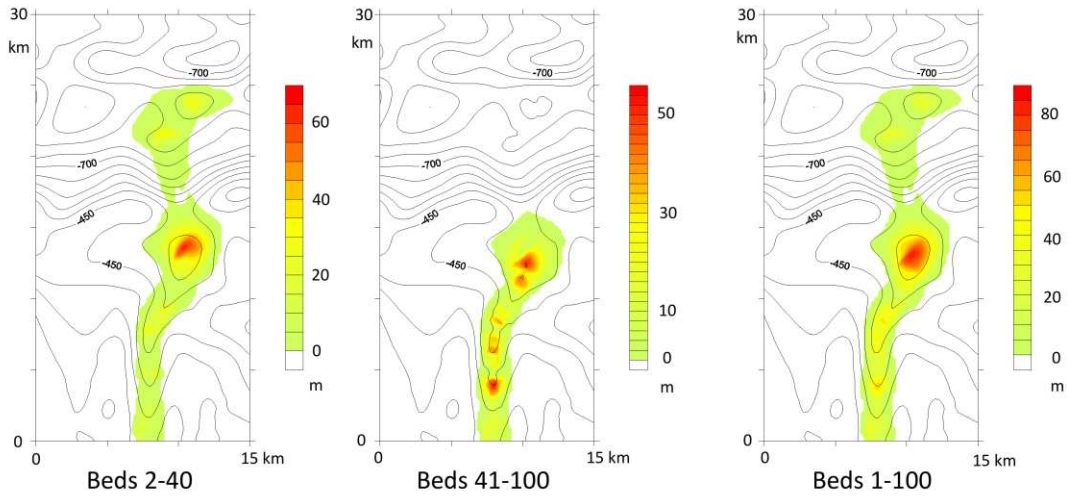
MODELLING THE STRATIGRAPHIC ARCHITECTURE OF MINIBASINS



941

942 **Figure 5**

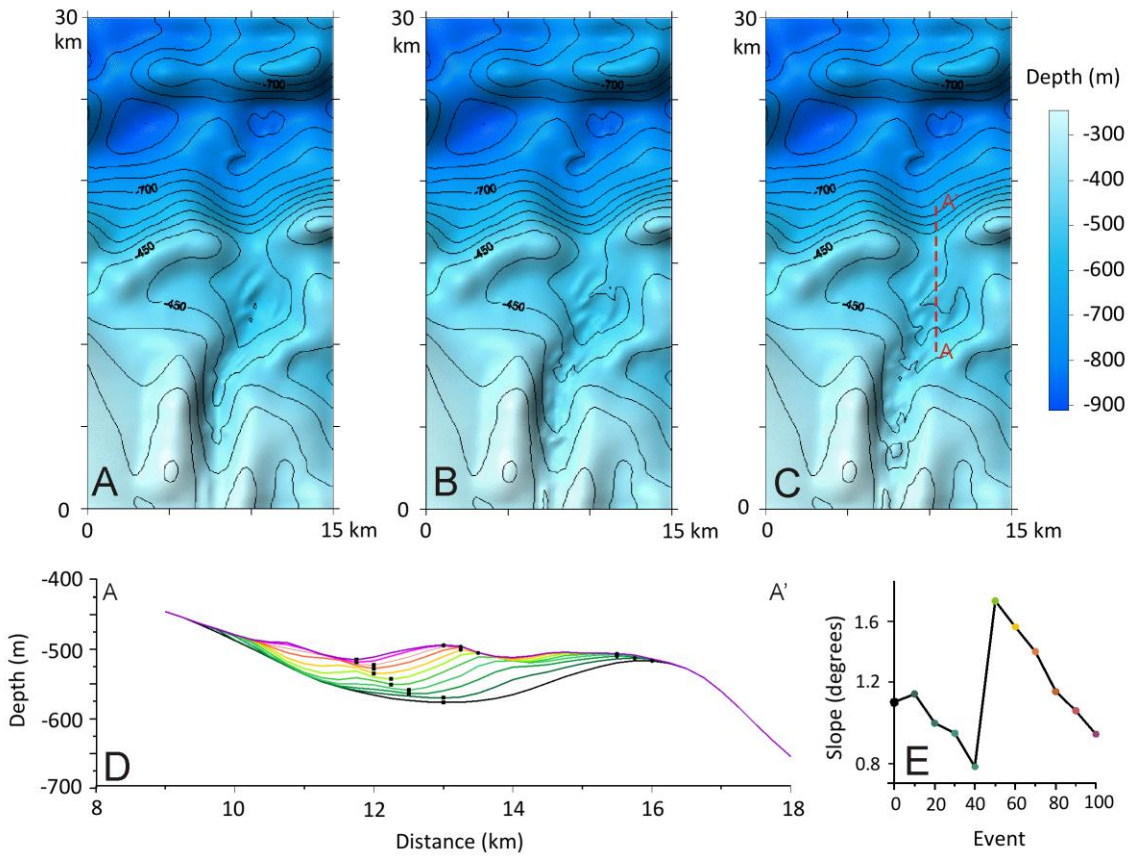
943



944

945 **Figure 6**

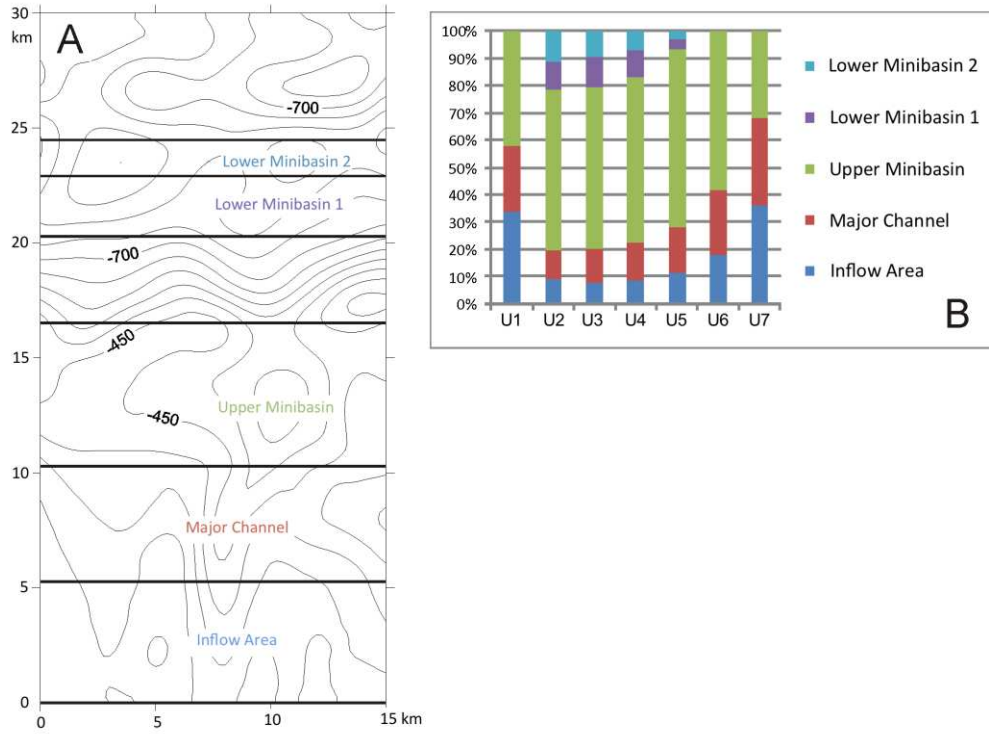
946



947

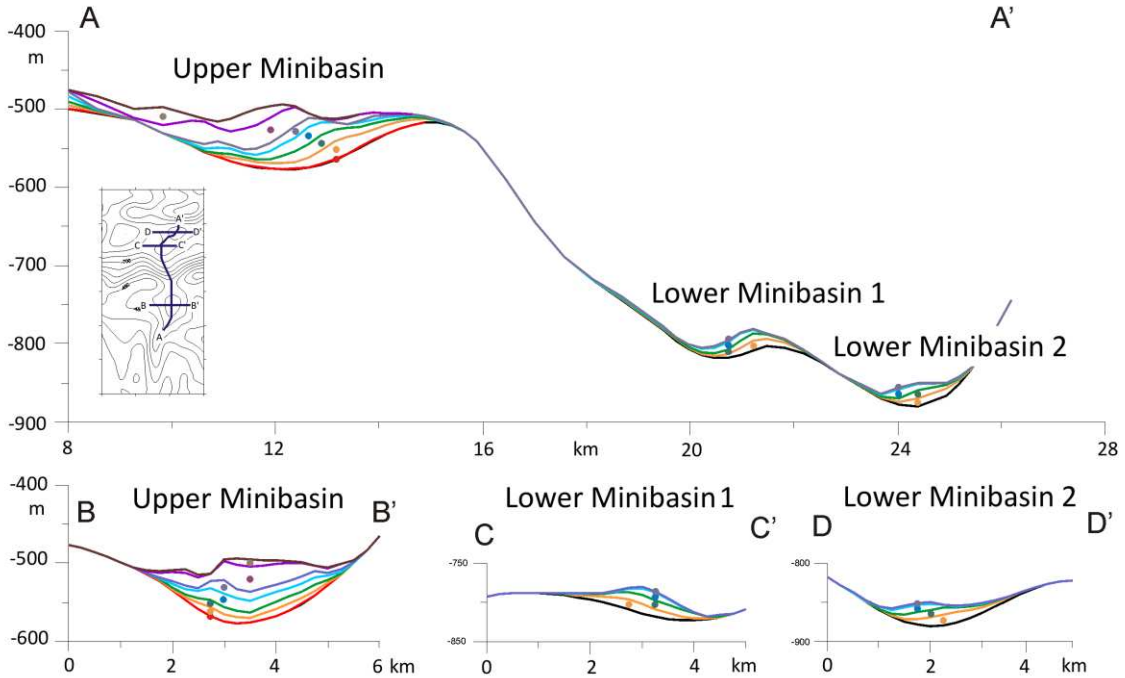
948 **Figure 7**

MODELLING THE STRATIGRAPHIC ARCHITECTURE OF MINIBASINS



949

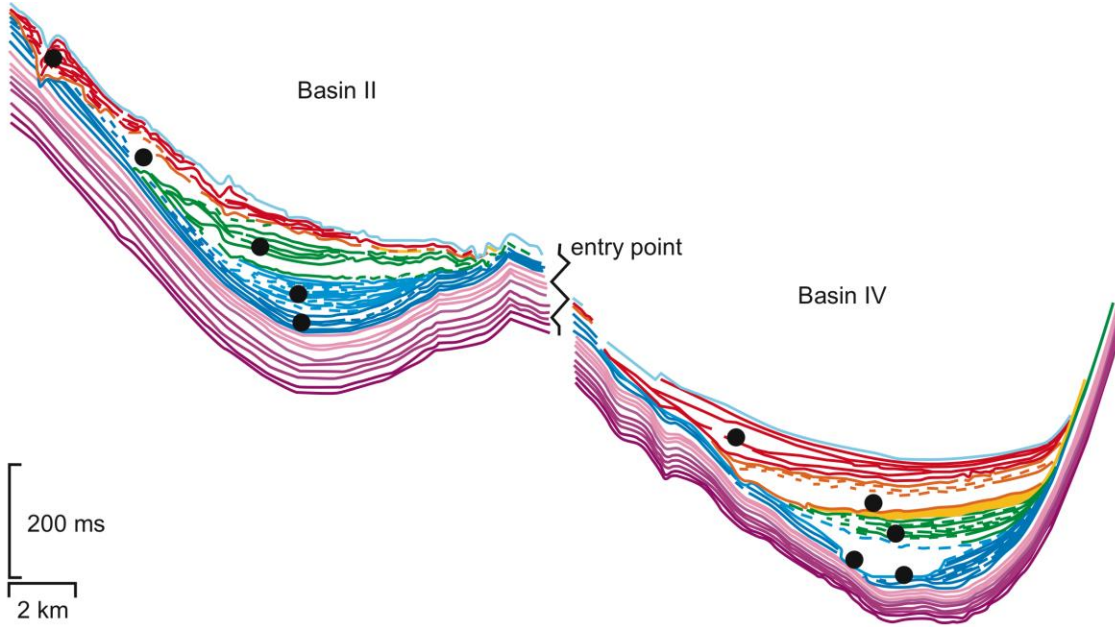
950 **Figure 8**



951

952 **Figure 9**

953



954

955 **Figure 10**

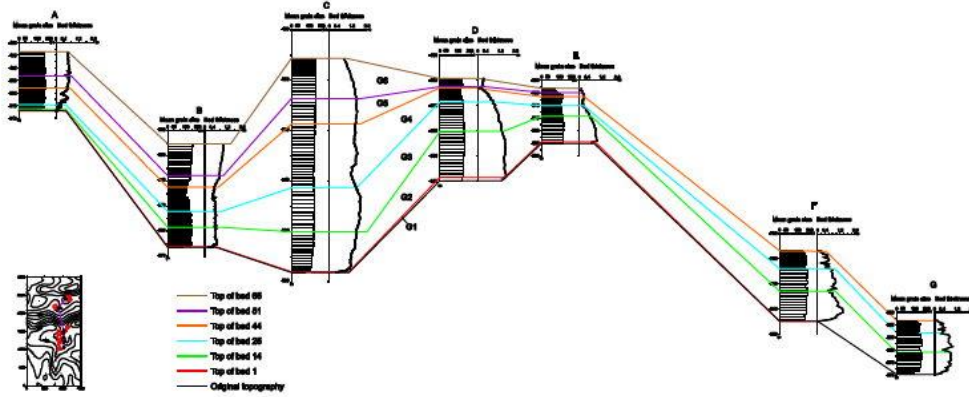


**Figure 5.12:** Cross-section showing the longitudinal isochronous correlation of the stratigraphy (supercritical non-equilibrium inflows) in the three minibasins. Seven spots are selected to display the mean grain-size column and layer thickness profile. Spots A, B, C and D are along the central longitudinal axis of the upper well-confined minibasin, spot F is located at the thickest deposit of the first lower minibasin, and spot G is in the second lower minibasin (see the map showing these locations). Six stratigraphic groups are recognized (G1, G2, G3, G4, G5 and G6). For detailed explanations see text.

956

957

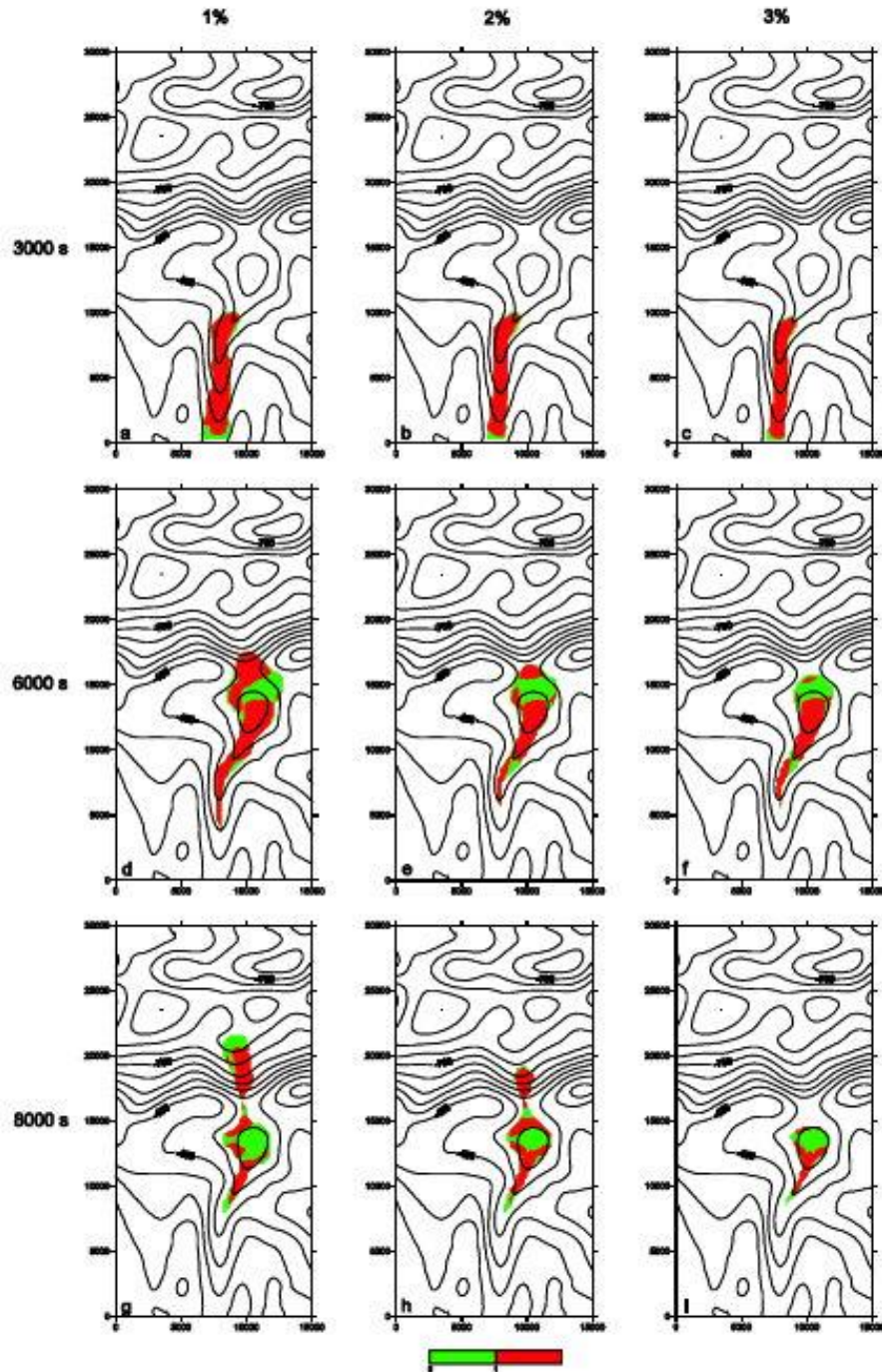


Figure 5.30: Densimetric Froude number evolution of event 2 (at 3000s, 6000s and 8000s) of the first group of subcritical equilibrium inflows (1%, 2% and 3%). All maps are superposed onto the elevation contour map of the original topography.